

PAPER • OPEN ACCESS

How electromagnetic stirring influences fluid flow in continuous casting of steel

To cite this article: Jakob Fainberg *et al* 2023 *IOP Conf. Ser.: Mater. Sci. Eng.* **1281** 012030

View the [article online](#) for updates and enhancements.

You may also like

- [Simulation of temperature field of A356 aluminum alloy in freeze casting](#)
Haoqin Yang, Zhongde Shan, Yifei Wang et al.
- [MCWASP XIII: International Conference on Modeling of Casting, Welding and Advanced Solidification Processes](#)
Andreas Ludwig
- [Mould design optimisation by FEM](#)
O Ayer and O Kaya



PRIME™
PACIFIC RIM MEETING
ON ELECTROCHEMICAL
AND SOLID STATE SCIENCE

HONOLULU, HI
October 6-11, 2024

Joint International Meeting of
The Electrochemical Society of Japan (ECSJ)
The Korean Electrochemical Society (KECS)
The Electrochemical Society (ECS)

Early Registration Deadline:
September 3, 2024

**MAKE YOUR PLANS
NOW!**

How electromagnetic stirring influences fluid flow in continuous casting of steel

Jakob Fainberg, Erik Hepp and Evgenii Shvydkii

MAGMA Gießereitechnologie GmbH, Kackertstr. 16-18, 52072 Aachen, Germany

E-mail: J.Fainberg@magma-soft.de, E.Hepp@magma-soft.de, E.Shvydkii@magma-soft.de

Abstract. State-of-art simulation models provide quantitative insights into flow, solidification and stress formation for continuous casting processes. This includes the entire process, from the tundish and the flow into the mold to the solidifying strand, which is withdrawn through various cooling zones. Process simulation and optimization provides important information about quality and productivity to evaluate process alternatives. This is only possible if all relevant process parameters can be taken into account. The use of electromagnetic stirring is a technology which plays a significant role in the majority of continuous casting processes worldwide and its effects cannot be neglected in simulation models. This paper will discuss the modeling of electromagnetic stirring (EMS) and its impact on steel slab continuous casting.

Two cases with and without EMS are presented. The theoretical background to calculate the Lorentz force are described. The EMS calculation described here works with traveling (linear) magnetic fields. The effect of the EMS on the flow behavior, solidification and macrosegregation is shown on an industrial-scale slab casting.

This information leads to a better understanding of the EMS process in industrial applications to avoid casting defects, improve the quality of the final product, and increase the efficiency of the casting process.

1. Introduction

Continuous casting is a crucial process for steel production. Over 96% of the globally produced raw steel is continuously-cast steel [1]. At the same time steel continuous casting is a sophisticated technological process. It involves a complex system of inter-related phenomena, such as for example turbulent liquid metal flow, heat transfer issues, solidification and microstructure formation. This multiphysical nature in combination with a large scale of industrial casters makes this process challenging for computational modelling. The state of the art of continuous casting numerical simulation is summarized in [2–4]. Although much progress is made, accurate defect prediction is still in its beginning.

Macrosegregation is one of these defects in continuous-cast steel. Moreover it is the most serious because macrosegregation cannot be removed by heat treatment as diffusion in solids is slow even for elevated temperatures and large diffusion distances might result in impracticably long holding times for homogenization. [5]. Modeling of macrosegregation is expensive due to the need to compute the transport of multiple chemical species. Most macrosegregation models for continuous casting use simplified binary alloy systems. However cast steels are multicomponent systems [6].

Other models are needed to include electromagnetics. Implementation of electromagnetic



fields has several applications in continuous casting [7]. It enables a contactless control of the fluid flow to improve quality and avoid defects in continuous cast steel slabs. Electromagnetic stirring inserted into the mold (M-EMS) was initially introduced to improve surface and subsurface quality. Control of the shell thickness allows to increase the casting speed as well. Moreover M-EMS prevents the superheat penetration deep down into the strand, thereby prolongs the mushy zone and promotes equiaxed crystal growth [8, 9].

Coupling together of different phenomena as macrosegregation and electromagnetics into multiphysics models remains a challenge [2]. The aim of this work is to illustrate the use of combined macrosegregation and EMS simulation by means of ready to use commercially available software. This work mirrors the actual state of continuous casting numerical simulation in the framework of MAGMASOFT[®] and MAGMA CC [10].

2. Method

2.1. Electromagnetic formulation

The Lorentz force appears in electric conductors imposed into a time dependent electromagnetic field. The flow in the metallic melt is driven among other things by the Lorentz force. This volumetric force results basically from interaction between the induced electric eddy current in the melt and the external magnetic field, both time dependent in the considered case. The Lorentz force is superimposed with other effects such as the thermal buoyancy and the forced flow due to the mass inflow and due to the strand withdrawal. In this work, the Lorentz force is computed from the solution of the complete Maxwell equation set. The Maxwell equations are formulated in terms of vector and scalar potentials for the frequency, or quasi-static domain and follow mainly the procedure described in [11]. It is assumed that the imposed electric currents in the inductors are harmonic with a prescribed amplitude and phase shift. Then, it is assumed that all field quantities Φ have the harmonic time dependence with the cyclic frequency of inductor currents due to linearity of the Maxwell equations.

$$\Phi = \Phi^{Re} \cos(\omega t) + i\Phi^{Im} \sin(\omega t) \quad (1)$$

Φ is a complex amplitude with two components (Φ^{Re} , Φ^{Im}), which are the in phase and out of phase components. The Maxwell equations are formulated in the frequency domain, which means that the time derivative is eliminated from them.

A vector potential A and a scalar potential ϕ are introduced as primary variables.

$$A = \vec{A}^{Re} + i\vec{A}^{Im} \quad (2)$$

$$\phi = \phi^{Re} + i\phi^{Im} \quad (3)$$

The considered Maxwell equations in the frequency domain are

$$\nabla \times E - i\omega\mu\mu_0 H = j_0 \quad (4)$$

$$\nabla \times H - (\sigma - i\omega\varepsilon)E = 0 \quad (5)$$

The local amplitude of the current density j_0 in the inductors is given by the total electric current amplitude defined for each inductor. It is assumed that there is no electric charge accumulation, and the magnetic permeability within a material is constant. Additionally to the equations (4) and (5), the definition of the magnetic induction B (6) is used:

$$B = \mu\mu_0 H \quad (6)$$

The complex potentials are defined in the unusual form as taken from [11]

$$E = A\nabla\phi \quad (7)$$

$$\nabla \times A = i\omega\mu H \quad (8)$$

The potential definitions in form (7) and (8) are inserted into the Maxwell equations (4)-(5) formulated in frequency domain (4) and (5). Then they are transformed with usage of the Coulomb gauge condition for the vector potential $\nabla A = 0$, and the resulting elliptic equations for unknown potentials in the frequency domain are obtained, in the electrically conducting domain

$$\nabla^2 A + i\omega\mu\mu_0\sigma(A + \nabla\phi) = -i\omega\mu j_0 \quad (9)$$

$$\nabla(\sigma A) + \nabla(\sigma\nabla\phi) = 0 \quad (10)$$

and else

$$\nabla^2 A = -i\omega\mu j_0 \quad (11)$$

The equations (9) and (10) describe the unknown complex vector A with 6 scalar components and the unknown complex scalar ϕ with 2 scalar components. 8 scalar equations and 8 unknowns result from (9) and (10). The electrically conducting domain consists of the solidified metal, the melt and optionally the permanent mold, all other materials are treated being not electrically conducting and are described by equation (11).

The boundary condition at the external boundary of the computational domain for all particular scalar equations are of Neumann type, i. e. no flux. There is a significant formulation drawback, the magnetic permeability μ cannot be discontinuous. In reality, the piecewise constant distribution of the permeability is more appropriate because of the jumps at the boundary between magnetic and non-magnetic materials. These jumps could not be taken into account in the actual formulation, hence bunching and amplifications of the magnetic field has to be approximated by the adjustment of electric current in the inductors. In order to overcome this limitation and allow a spatial jump of the magnetic permeability, the formulation has to be modified in future.

The equations are discretized according to the finite volume method on a Cartesian grid. The matrix of the total equation system consists of the 8×8 blocks associated with the particular elliptic equations and with the cross-terms proportional to the coupling parameter.

$$\nabla^2\Phi = 0 \quad (12)$$

The potential equation is a Laplace one for the computational domain consisting of the single inductor. The boundary conditions are symmetry everywhere excepted at the contact areas with electrodes. The Dirichlet boundary conditions are applied at both contact areas with cathode and anode. The Dirichlet value unity is prescribed at the cathode and zero at the anode.

The local current density is computed from the solution of (12). The gradient of the obtained potential is scaled with a constant factor K to obtain the current density accordingly to the input of the inductor current. The current is the surface integral of the unknown current density over the contact area between the inductor and cathode. Hence

$$K = \frac{I}{S|\nabla\Phi|} \quad (13)$$

with I the prescribed inductor current, S the contact area between the inductor and cathode and $|\nabla\Phi|$ the absolute value of potential gradient at the contact with the cathode. The obtained current density is then

$$j = K\nabla\Phi \quad (14)$$

2.1.1. Electromagnetic computational domain and the solution procedure. The calculation of the continuous casting process with electromagnetic stirring is split internally into two steps. In the first step, the Lorentz force associated with each stirring device is computed and stored. In the second one, the Lorentz forces from all available active stirrers are applied to the computational fluid dynamics within the melt. The requirements on the grid resolution of electromagnetic and thermally coupled CFD computations can be strongly different, and the region affected by the electromagnetic field in vicinity of the stirrer takes usually only a small part of the total computational domain. Hence the trial to compute both problems on the same grid would lead to a huge numerical grid and extensive computational time of the continuous casting process.

Therefore, the electromagnetic computation is completely separated from the continuous casting computational process and computed on a separate grid.

The CAD preprocessor allows to define an arbitrary number of stirrers which includes a number of elements such as inductors, electrodes and magnetic cores. The definition of a single stirring region is illustrated in Fig. 1.

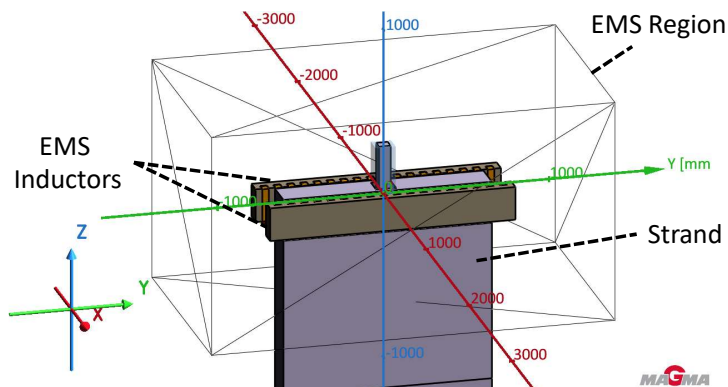


Figure 1. Definition of a single stirring region. The geometrical components, the size of the stirrer region and its location either in absolute coordinates or with respect to the strand are prescribed.

The computational process starts from creation of the project subversion for electromagnetic computation, the grid generation for the considered EMS region and the solution of equations (12) and (9)-(11). All these steps are executed for each available active electromagnetic region automatically based on the geometric and other definitions done in the basic continuous casting setup. The equation system can be effectively solved using the algebraic multigrid technique.

2.1.2. Lorentz force. The stored results are the time averaged Lorentz Force density and auxiliary results such as eddy current densities, magnetic induction and components of complex scalar and vector potentials. After results for all EMS regions are obtained, the computation is switched to the main part of the continuous casting process. The Lorentz force densities are read from the stored files of the particular computed EMS subversions and interpolated onto the actual grid used for the continuous casting fluid flow simulation. The interpolation is done in such a way that the volume integral over each component of the Lorentz force is preserved.

The Lorentz force is given as a cross product of the current density and the magnetic field, or

$$F_L = \sigma(E \times B) \quad (15)$$

Taking in account that each of E and B vectors changes harmonically with time, one obtains a harmonic and a constant components of (15). The harmonic component has a double frequency of the inductor current and is not accounted for in the acceleration of the flow. The constant component of the Lorentz force, returned by time averaging is applied as a momentum source term.

$$\langle F_L \rangle = \sigma \frac{1}{T} \int (E \times B) dt \quad (16)$$

The averaging via the integral (16) is applied for one period of the inductor current oscillation.

One obtains the following expression for Cartesian components of the Lorentz force after execution of integral (16)

$$\langle F_L \rangle = \frac{1}{2} \sigma \begin{pmatrix} E_y^{Re} B_z^{Re} + E_y^{Im} B_z^{Im} - E_z^{Re} B_y^{Re} - E_z^{Im} B_y^{Im} \\ E_z^{Re} B_x^{Re} + E_z^{Im} B_x^{Im} - E_x^{Re} B_z^{Re} - E_x^{Im} B_z^{Im} \\ E_x^{Re} B_y^{Re} + E_x^{Im} B_y^{Im} - E_y^{Re} B_x^{Re} - E_y^{Im} B_x^{Im} \end{pmatrix} \quad (17)$$

The real and imaginary components of the electric and magnetic fields E and B that are complex amplitudes are obtained directly from solution of the potential problem (9)-(11) according to definitions (6)-(8).

2.2. Species transport

The species transport in both liquid and solid phases has to be considered in the continuous casting configuration. The transport in the liquid phase differs from that in the solid phase by the macroscopic diffusion but its relative contribution is typically small in comparison with the convective transport. No relative velocity of the liquid and solid phase is considered, both phases are moved together. For the melt temperature above the predefined freezing temperature, the movement of the equiaxed crystals is assumed with the liquid phase velocity, no flotation or sedimentation is considered. Below the freezing temperature both phases are moved with the prescribed withdrawal velocity.

The formulation is based on the work of Schneider and Beckermann [6]. Species transport with segregation is considered for an arbitrary number of chemical elements in two phases, liquid and solid. Two transport equations are solved for each chemical element.

$$g_s \rho_s \frac{\partial C_s}{\partial t} + g_s \rho_s V_s \nabla C_s = \Gamma_{sl} (\kappa C_l - C_s) + S_v \rho_s D_s \frac{\kappa C_l - C_s}{l_{sl}} \quad (18)$$

$$g_l \rho_l \frac{\partial C_l}{\partial t} + g_l \rho_s V_l \nabla C_l = \nabla (g_l \rho_l D_l \nabla C_l) - \Gamma_{sl} (\kappa C_l - C_l) - S_v \rho_s D_s \frac{\kappa C_l - C_s}{l_{sl}} \quad (19)$$

The volume averaged species concentration in the liquid and solid phases are denoted as C_l and C_s , the volume liquid and solid phase fractions correspondingly g_l and g_s . The index of the considered chemical element is omitted in (18)-(19) for simplicity. The flow velocities in the liquid and solid phases are V_l and V_s . The temperature dependent partition coefficient is denoted as κ and the temperature dependent diffusion coefficients in two phases as D_l and D_s .

Γ_{sl} is the local solidification rate, computed via the total time derivative as

$$\Gamma_{sl} = \frac{\partial}{\partial t} (g_l \rho_s) + \nabla (g_s \rho_s V_s) \quad (20)$$

The ratio of the diffusion area to the diffusion length in the back diffusion term is approximated as

$$\frac{S_v}{l_{sl}} = \frac{12}{d_2^2 g_s} \quad (21)$$

with d_2^2 quadrat of secondary dendrite arm spacing.

The transport and segregation of 7 chemical elements was considered in this study. Chemical elements and their properties are shown in Table 1.

Table 1. Physical properties of the 18Cr-8Ni alloy components used for the simulations.

	[wt.%]	κ_s	κ_l	β_s [$\frac{1}{wt.\%} \cdot 10^{-3}$]	β_l [$\frac{1}{wt.\%} \cdot 10^{-3}$]	D_s [$\frac{m^2}{s} \cdot 10^{-14}$]	D_l [$\frac{m^2}{s} \cdot 10^{-13}$]
C	0.1	0.28	0.12	11.0	11.0	59000	10300
Si	1.0	1.21	0.97	17.9	18.1	630	160
Mn	1.0	0.84	0.73	2.7	3.1	4.8	1.8
Cr	18.0	0.74	1.00	0.74	0.63	2800	1100
Cu	1.0	0.68	0.43	-0.76	-0.89	10	1.0
Mo	0.5	0.51	0.95	-2.8	-3.1	7.8	22
Ni	8.0	1.14	0.81	-0.1	-0.87	3.2	1.1

Table 1 contains properties for 7 considered chemical elements in the 18Cr-8Ni alloy. C_{in} is the initial element concentration. Partitioning coefficients κ , volumetric expansion coefficient β and solid state diffusion coefficient are given at liquidus and solidus temperatures. Hence, the partitioning coefficient is given at the liquidus (κ_l) and solidus (κ_s) temperatures. The coupling with fluid flow is given via solutal buoyancy by means of the volumetric expansion coefficient β .

2.3. Reference case

As a reference case the work of Kihara et al. [12] is chosen. The authors simulated a slab continuous casting for austenitic stainless steel and experimentally validated it. The caster is supplemented by a mold electromagnetic stirrer (M-EMS) which is aimed to avoid a negative segregation underneath the slab surface.

Geometry of the chosen case is partially shown in figure 1. The 35.8 m long strand has a cross section of 200×1258 mm and a bow radius of 10 m. M-EMS consists of two travelling magnetic field inductors placed at the strand wide sides near the meniscus.

The applied numerical mesh consists of totally 1,243,702 cartesian cells. The mesh is refined in z -direction at the mold area and in the expected position of the wall boundary layers along the whole strand.

Heat transfer coefficients are set according to [12]. Primary cooling coefficient at the mold area h_{mold} is $1200 \text{ W/m}^2\text{K}$, secondary cooling $h_{secondary} = 418 \text{ W/m}^2\text{K}$ and the meniscus $h_{meniscus} = 52 \text{ W/m}^2\text{K}$. The start melt temperature $T_{in} = 1492^\circ\text{C}$ which means a superheat of 45°C . The casting speed $v_{cast} = 1.2 \text{ m/min}$, this corresponds to a maximum velocity in the SEN of $v_{SEN} \approx 0.96 \text{ m/s}$

3. Results

The Lorentz force is calculated before the thermal and fluid flow simulation starts. Figure 2 shows the distribution of these induced forces on the slab cross section. Two travelling magnetic field inductors generate forces along the slab wide faces. Due to the skin effect these forces are located near the surface and do not penetrate into the middle of the slab. Direction of forces on lower surface in figure 2 is opposite to the upper, thus a counterclockwise torque is produced. The maximum value is about 5000 N/m^3 which corresponds to the reference case in [12].

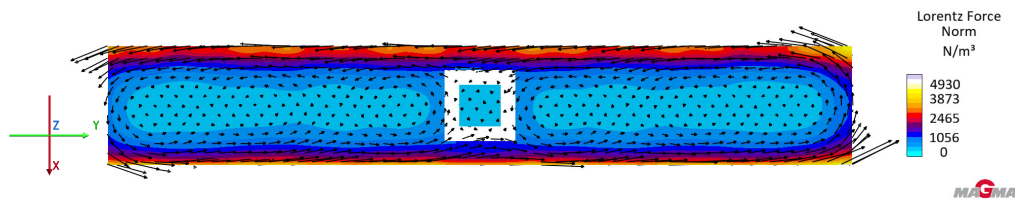


Figure 2. Lorentz forces

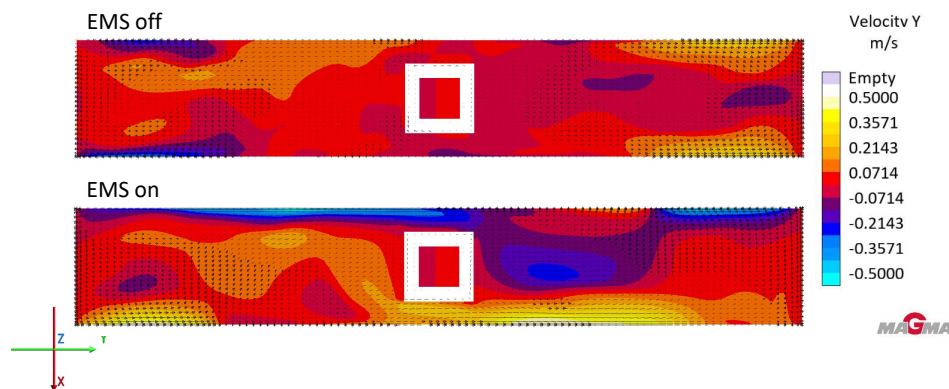


Figure 3. Velocity y -component at the 100 mm from the meniscus for 1400 s.

The velocity distribution at the middle height of the EMS inductors is shown in figure 3. The EMS forces the fluid flow in the horizontal plane of the strand. The EMS generates a positive y -component velocity at the bottom face as shown in figure 3 and negative at the opposite face. Thus a counterclockwise flow pattern occurs. Without EMS, the flow pattern is dominated by jets from the submerged entry nozzle (SEN) and is symmetric.

Figure 4 shows a flow pattern by streamlines. There is a conventional four-vortex flow pattern controlled by the SEN jets without EMS. Whereas electromagnetic forces generate the superimposed rotation about the vertical axis z . Electromagnetically driven flow appears near the meniscus where the EMS is placed.

This has an effect on the temperature field in the strand. The strand surface temperature is shown in figure 5. The temperature gradually decreases in the withdrawal direction and reaches $\sim 500^\circ\text{C}$ at the surface of the horizontal part due to primary and secondary cooling. EMS shifts isotherms which results in a non-symmetric temperature distribution comparing with the reference case without EMS.

Next important parameter is the solidified shell thickness. Liquid fraction in the slab cross section is shown in figure 6. The solidified shell stays symmetrical without EMS. It became thicker in the slab corners and in the middle slab faces with EMS. The applied EMS deforms the solidified shell. It thins the shell at upper right and lower left positions of the slab cross section by means of superheat advection. The metallurgical length is 16.96 m without EMS case and 17.34 m for the case with EMS.

The distribution of the averaged slab shell thickness along the strand length is shown in the figure 7. Results with and without EMS match well within the first strand interval of 300 mm. Below this interval, EMS produces a thinner shell compared with the case without EMS. Intensive stirring keeps superheat in the upper mold part preventing its penetration deep down into the strand. The difference in the obtained shell thickness is about 3 mm and remains

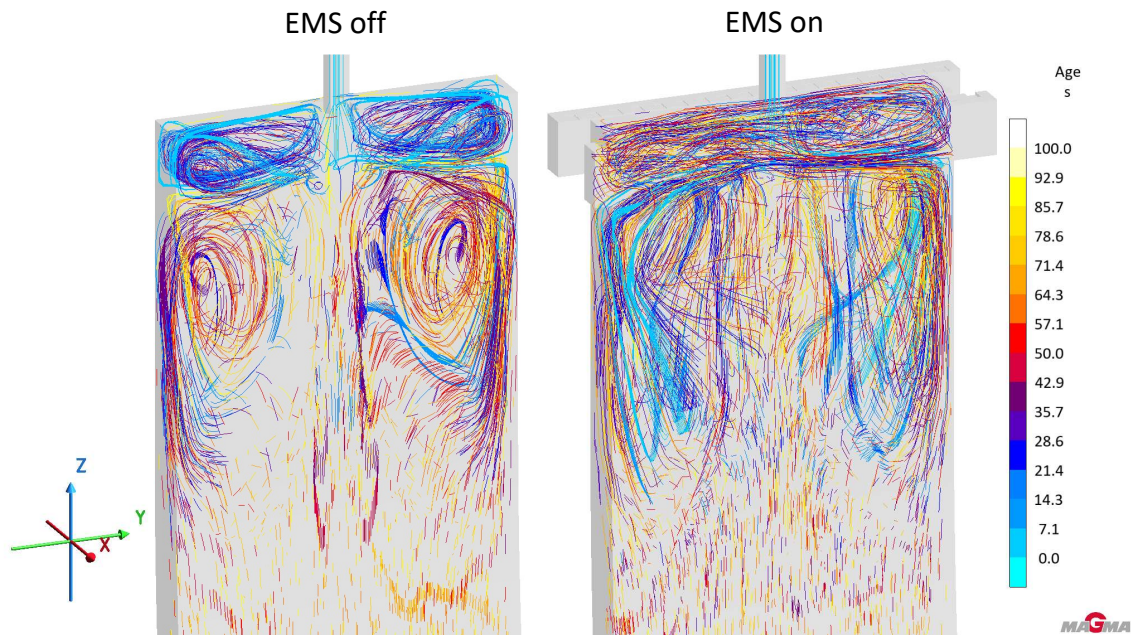


Figure 4. Flow pattern streamlines

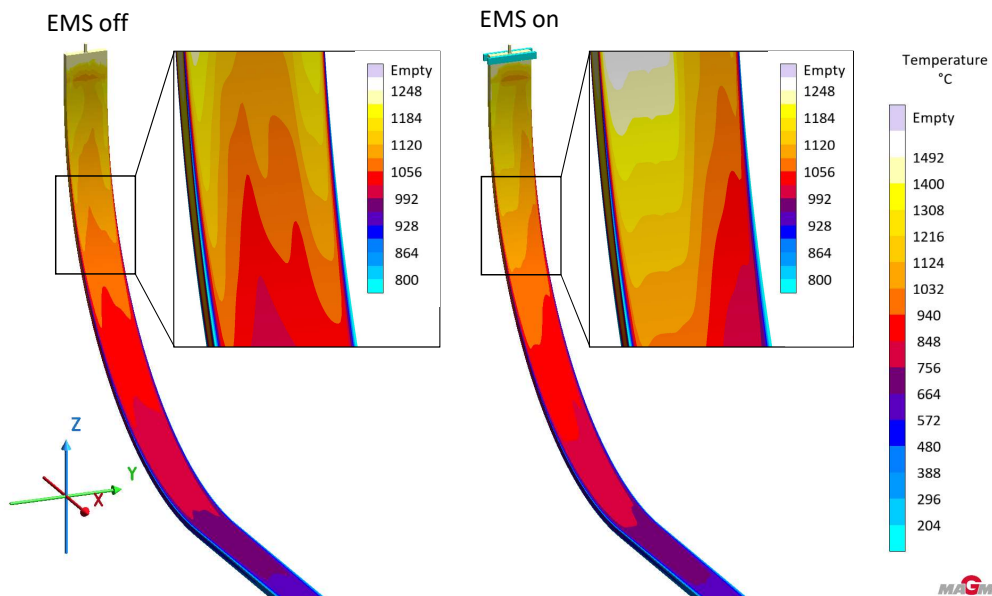


Figure 5. Strand surface temperature.

constant along the strand length.

Figure 8 shows concentration distribution in the slab cross section for the considered chemical alloy elements. The results are evaluated at the end of simulation at 30 minutes of the process time, in the strand cross section located just after the metallurgical length position at 18 m of strand length. Left column is without EMS and right one with EMS. The most prominent segregation is observed for the Carbon, due to the lower value of its partition coefficient (see

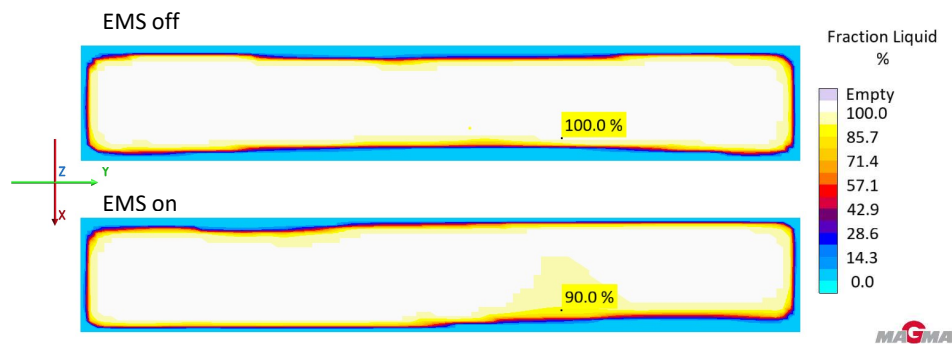


Figure 6. Liquid fraction at the 2300 mm from the meniscus.

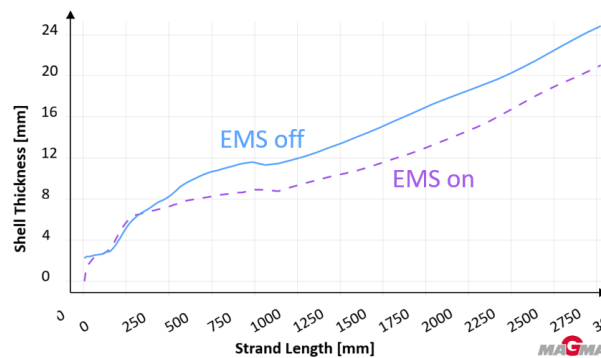


Figure 7. Averaged shell thickness over the strand length.

table 1). Almost no macrosegregation for Si is obtained in opposite to Carbon.

Electromagnetic stirring significantly affects the C and Cr distribution. The stirring in the plane of the strand cross section transports the solute to the upper right and the lower left corners and increases the Carbon concentration up to 0.15% there. The concentration pattern remains more symmetric without EMS. In addition, EMS eliminates the negative segregation spot at the center of the slab for Mn, Mo and Ni elements.

4. Conclusion

A global numerical model for stainless steel slab continuous casting is presented. Two cases with and without EMS are considered. The influence of EMS forced flow on temperature field, solidified shell and macrosegregation is shown. The longitudinal temperature distribution along the strand length changes by EMS. This is due to the effect of the enhanced superheat advection. EMS deforms the solid shell, breaks its symmetry and makes it thinner as well. The explicit effect of EMS is noticeable for the Carbon macrosegregation mainly. Other elements shows minor effects but for e.g. Cu, Mo and Ni concentration distribution is more uniform in the EMS case.

The presented model is a commercially available tool to simulate the continuous casting process at industrial scale. The temperature field, fluid flow, solidification and macrosegregation are computed simultaneously, in 3D and transient. Moreover, electromagnetic field calculation is incorporated into the computational workflow in an automatic way to enable an easy calculation of the electromagnetic stirring. Demonstrated cases are computed with standard PC in parallel mode with 32 cores. The computational time was about 32 hours.

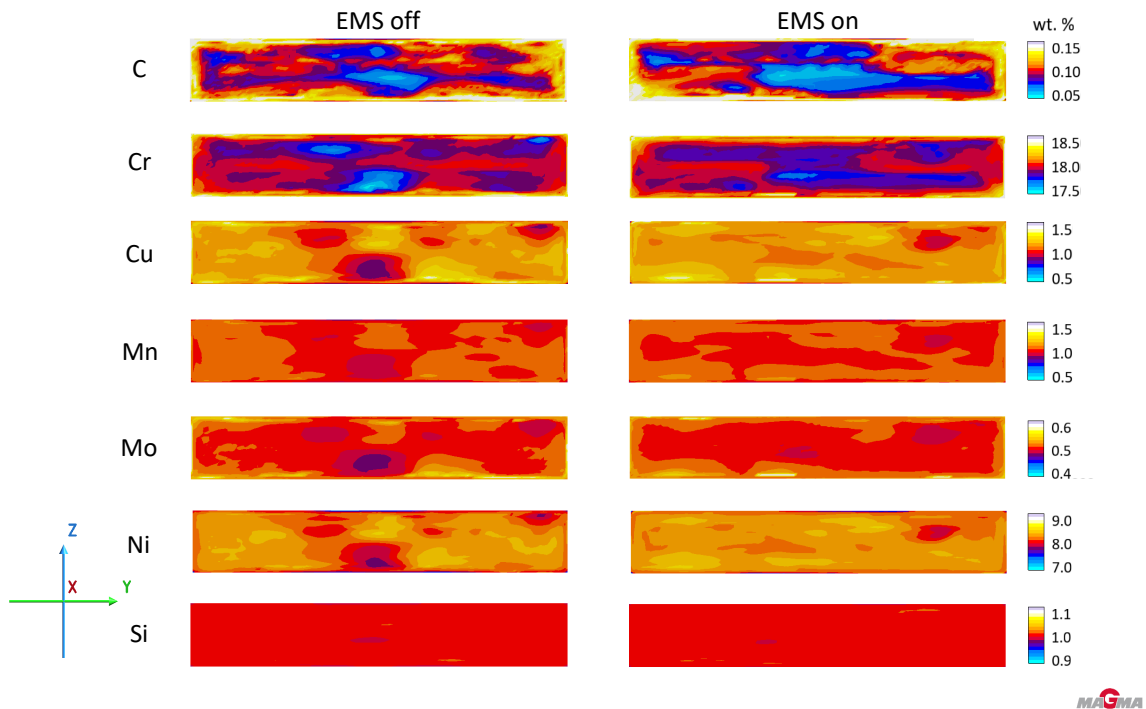


Figure 8. Distribution of the concentration for 7 chemical elements in the slab cross section at the position of 18 m of the strand length.

References

- [1] Steel statistical yearbook 2018 <https://worldsteel.org/wp-content/uploads/Steel-Statistical-Yearbook-2018.pdf>
- [2] Thomas B G 2018 *steel research international* **89** 1700312 URL <https://doi.org/10.1002/srin.201700312>
- [3] Miłkowska-Piszczek K and Falkus J 2018 *Metals* **8** ISSN 2075-4701 URL <https://www.mdpi.com/2075-4701/8/8/591>
- [4] Vynnycky M 2018 *Metals* **8** ISSN 2075-4701 URL <https://www.mdpi.com/2075-4701/8/11/928>
- [5] Ludwig A, Wu M and Kharicha A 2015 *Metallurgical and Materials Transactions A* **46** 4854–4867 URL <https://doi.org/10.1007/s11661-015-2959-4>
- [6] Schneider M C and Beckermann C 1995 *Metallurgical and Materials Transactions A* **26** 2373–2388 URL <https://doi.org/10.1007/bf02671251>
- [7] Cho S M and Thomas B G 2019 *Metals* **9** ISSN 2075-4701 URL <https://www.mdpi.com/2075-4701/9/4/471>
- [8] Kunstreich S 2003 *Revue de Métallurgie* **100** 395–408 URL <https://doi.org/10.1051/metal:2003198>
- [9] Kunstreich S 2003 *Revue de Métallurgie* **100** 1043–1061 URL <https://doi.org/10.1051/metal:2003113>
- [10] Fainberg J, Hepp E, Schäfer W and Kraftthöfer C 2020 *IOP Conference Series: Materials Science and Engineering* **861** 012017 URL <https://dx.doi.org/10.1088/1757-899X/861/1/012017>
- [11] Aruliah D A, Ascher U M, Haber E and Oldenburg D 2001 *Mathematical Models and Methods in Applied Sciences* **11** 1–21 URL <https://doi.org/10.1142/s0218202501000702>
- [12] Kihara K, Okada N, Saito S and Kawashima K 2022 *ISIJ International* **62** 1862–1873 URL <https://doi.org/10.2355/isijinternational.ISIJINT-2022-120>